A topology optimization method for hyperelastic porous structures subject to large deformation

Jiaqi Huang · Shuzhi Xu · Yongsheng Ma · Jikai Liu

Abstract Porous infill, rather than the solids, can provide high stiffness-to-weight ratio, energy absorption, thermal insulation, and many other outstanding properties. However, porous structure design to date have been majorly performed with topology optimization under small deformation assumption. The effect of porosity control under large deformation is not explored yet. Hence, this paper exploits the topological design method of porous infill structures under large deformational configuration. Specifically, the neo-Hookean hyperelasticity model is adopted to simulate the large structural deformation, and the adjoint sensitivity analysis is performed accordingly with the governing equation and constraint. The maximum local volume fractions before and after deformation are concurrently constrained and especially for the latter, the representative volume points (RVPs) are modeled and tracked for evaluating the local volume fractions subject to the distorted mesh configuration. The local volume constraints are then aggregated with the P-norm method for a global expression. Iterative corrections are made to the P-norm function to rigorously restrict the upper bound of the maximum local volume. Finally, several benchmark cases are investigated, which validate the effectiveness of the proposed method.

Keywords Porous infill · Nonlinear analysis · Hyperelastic material · Topology optimization · SIMP

J. Huang · J. Liu (✉)
Center for Advanced Jet Engineering Technologies
(CaJET), Key Laboratory of High Efficiency and Clean
Mechanical Manufacture (Ministry of Education), School
of Mechanical Engineering, Shandong University, Jinan,
China
e-mail: jikai_liu@sdu.edu.cn

S. Xu · Y. Ma
Department of Mechanical Engineering, University of
Alberta, Alberta, Canada

J. Liu
Key National Demonstration Center for Experimental
Mechanical Engineering Education, Shandong University,
Jinan, China

1 Introduction

Topology optimization has been extensively studied in the past three decades since the remarkable work by Bendsøe and Kikuchi (Bendsøe and Kikuchi 1988). It provides a robust and capable tool for optimal structural design while complying the specific boundary conditions and domain restrictions. Nowadays, topology optimization has been recognized and widely adopted in both academia and industry. As an emerging aspect of topology optimization, porous infill design has attracted a great deal of attention, which has the potential to exhibit high stiffness-to-weight ratio, energy absorption, thermal insulation,

and other outstanding properties that are non-achievable by the solids (Liu et al. 2018).

Given the specific methods for porous structure design, a routine approach is to investigate the microstructures through homogenization. The homogenization-based scheme builds the cross-scale connection by bridging the microscopic structures and the macroscopic equivalent material properties (Zhang et al. 2021a, b). At the early stage, the inverse homogenization method was developed to design unit microstructures exhibiting maximum shear and bulk moduli (Huang et al. 2011; Sigmund 2000), outstanding buckling strength (Wang and Sigmund 2020), negative Poisson's ratio (Andreassen et al. 2014), etc. Moreover, the unit microstructures were also tailored to employ excellent physical features, including magnetic and electrical permittivity (Huang et al. 2012), fluid permeability (Guest and Prévost 2006), acoustic wave propagation (Zhang et al. 2021a, b) and others. Later, beyond the unit cell optimization, methods were developed to support the concurrent macroscopic topology and microscopic porous infill design (Guo et al. 2015; Yan et al. 2016; Xu et al. 2021a, b). The cross-scale sensitivity information is established on the microscopic density variables by solving the homogenization and adjoint equations. The approaches are classified into optimization with parameterized unit cell microstructures and optimization with freeform unit cell microstructures with restricted or unrestricted material distribution, connectivity, and orientation conditions (Wu et al. 2021). So far, most of researches are focused on linear material elastic model under small deformation assumption. Trials on nonlinear porous infill or microstructure design were rarely attempted. Behrou et al. (Behrou et al. 2021) designed periodical microstructures exhibiting prescribed constitutive model under certain large strain state considering the geometric nonlinearity. Wang et al. (Wang 2018; Wang et al. 2014b) designed the auxetic meta-materials based on the hyperelastic fundamental material model to enable the structure demonstrating prescribed nonlinear properties. Other works also addressed the meta-material or multi-scale structural topology optimization incorporating the elastoplastic (Kim and Yun 2020), viscoelastic (Huang et al. 2015), elastoviscoplastic (Fritzen et al. 2016) nonlinear material models.

Recently, an alternative approach for porous infill design was developed and widely followed which employ sufficiently fine mesh and maximum local material fraction constraints to achieve the 'multi-scale' design effect with controlled porosity distribution. Wu et al. (Wu et al. 2018) originally proposed the idea and applied it to shell-infill structure design (Wu et al. 2017). In the above work, the local volume fraction constraints were aggregated into a global expression through P-norm method, but the local porosity constraints cannot be strictly satisfied with the static P-norm approximation. Later, the above method was extended to design functionally-graded (Liu et al. 2021; Schmidt et al. 2019), multi-material (Li et al. 2020), and thermal dissipation (Das and Sutradhar 2020) porous infills. In an alternative approach, Dou (Dou 2020) incorporated the maximum local volume requirement into the material interpolation model by customizing two layers of filtering and projection operations, which also achieved the porous infill design effect with controlled porosity. So far, the above mono-scale porous infill designs were all conducted based on linear elasticity assumption, while the extension to nonlinear structures was rarely targeted.

In fact, macroscopic topology optimization based on geometric nonlinearity or hyperelasticity has been addressed with different branches of topology optimization methods, including level set (Chen et al. 2017; Ha and Cho 2008), bi-directional evolutionary structural optimization (BESO) (Han et al. 2021), Solid Isotropic Material with Penalization (SIMP) (Ortigosa et al. 2020; Zheng et al. 2015), etc. A severe issue happens to the low-density elements that are prone of excessive deformation, incurring structural instability of the Newton–Raphson procedure. Buhl et al. (Buhl et al. 2000) relaxed the convergence criteria during the FEA process. Bruns and Tortorelli (Bruns and Tortorelli 2003) proposed the element removal and reintroduction technique to overcome the problem. To enable larger deformation, Wang et al. (Wang et al. 2014a) modified the energy interpolation model by assigning linear model to low density elements. Luo et al. (Liu et al. 2017; Luo et al. 2015) utilized the Yeoh hyperelastic model to avoid over distortion of the void elements. Moreover, Yoon and Kim (Yoon and Kim 2005) proposed an element connectivity parameterization (ECP) method, which applied zero length links between elements as design

variables that eliminates the low-density elements. van Dijk (van Dijk et al. 2014) applied the element deformation scaling (EDS) to project the local internal displacements into an acceptable range.

In this research, we propose a porous infill topology optimization method considering hyperelastic material behavior under the SIMP framework. The neo-Hookean hyperelasticity model is adopted to simulate the large structural deformation, and the adjoint sensitivity analysis is performed accordingly with the governing equation. To address the structural instability, the hyperelastic strain energy model is reformulated by incorporating the Heaviside-projected element densities to scale the element distortion. Another highlight was put on the maximum local volume fraction control. Previous works (Dou 2020; Wu et al. 2018, 2017) mainly concentrated on local porosity control subject to a fixed mesh and small mesh distortion, which is no longer valid for the large distortion cases. Hence, a new method was contributed for the maximum local volume fraction control under the large deformation scheme. This new method utilizes representative volume points (RVPs) to discretize the finite elements. Then, each RVP corresponds to a sub-element volume and the deformation trajectories of the RVPs are followed to track the changes of the sub-element volumes. In this way, the local material volumes can be accurately counted under any deformed mesh state. The maximum local volume constraint is established with the P-norm aggregation function to convert the large amounts of local volume constraints into one concise and differentiable expression. To ensure stability and close the gap between the P-norm approximation and the exact maximum local volume fraction, iterative corrections are made to the P-norm function (Long et al. 2019; Yang et al. 2018). Finally, for the numerical implementation, concurrently constraining the maximum local volume fractions before and after deformation is made possible.

The remaining part of this paper proceeds as follows: Sect. 2 demonstrates the details of introducing RVPs for local porosity estimation under deformed mesh state; Sect. 3 illustrates nonlinear finite element analysis, especially the neo-Hookean model for hyperelastic analysis; in Sect. 4, the topology optimization is established, and the sensitivity is calculated. To validate the proposed method, several benchmark examples are studied in Sect. 5. In the

last section, discussions and conclusions of this paper are provided.

2 Maximum local volume constraint

In this study, topology optimization for porous infill structures under large deformation is explored. The structural porosity is achieved by configuring maximum local volume fraction constraints and hence, properly counting the local material volume fraction is extremely important. Local volume fraction calculation is usually established on a fixed design domain discretized with quadrilateral elements. Each element is assigned a pseudo physical density $\overline{\overline{\rho}} \in (0, 1]$ and has the element volume $\tilde{v}$. In the undeformed state, the linearly interpolated material volume is expressed by:

$$v = \overline{\overline{\rho}}\tilde{v} \tag{1}$$

As illustrated in (Wu et al. 2018), the local material volume fraction is counted within a circular neighbourhood based on the percentage of solid elements against the total (Fig. 1a), through:

$$vf_e = \frac{\Sigma_{i\in N_e}\overline{\overline{\rho}}_i}{\Sigma_{i\in N_e}1} \tag{2}$$

where N_e is collection of elements inside the circular neighborhood of element e; see Fig. 1a. $\tilde{v}$ is a constant given the uniform mesh and the small deformation assumption and thus, is eliminated when formulating Eq. (2).

Apparently, Eq. (2) is not applicable to structures experiencing large deformation since the element sizes vary significantly alongside the structural deformation and some growing elements should be sub-discretized to increase the volume counting accuracy. Therefore, a new method for counting the local material volume fraction is developed in the current study by prescribing the local material volumes on RVPs (Representative Volume Points). As shown in Fig. 1b, the RVP is a smaller unit to capture the material distribution information. In case of sub-discretized into 9 RVPs, each RVP corresponds to 1/9 of the element volume and the exact percentage evolves according to the element distortion condition. Hence, the RVPs fine-tune the material volume counting and even for obviously growing elements, the RVPs keep a good approximation of the local
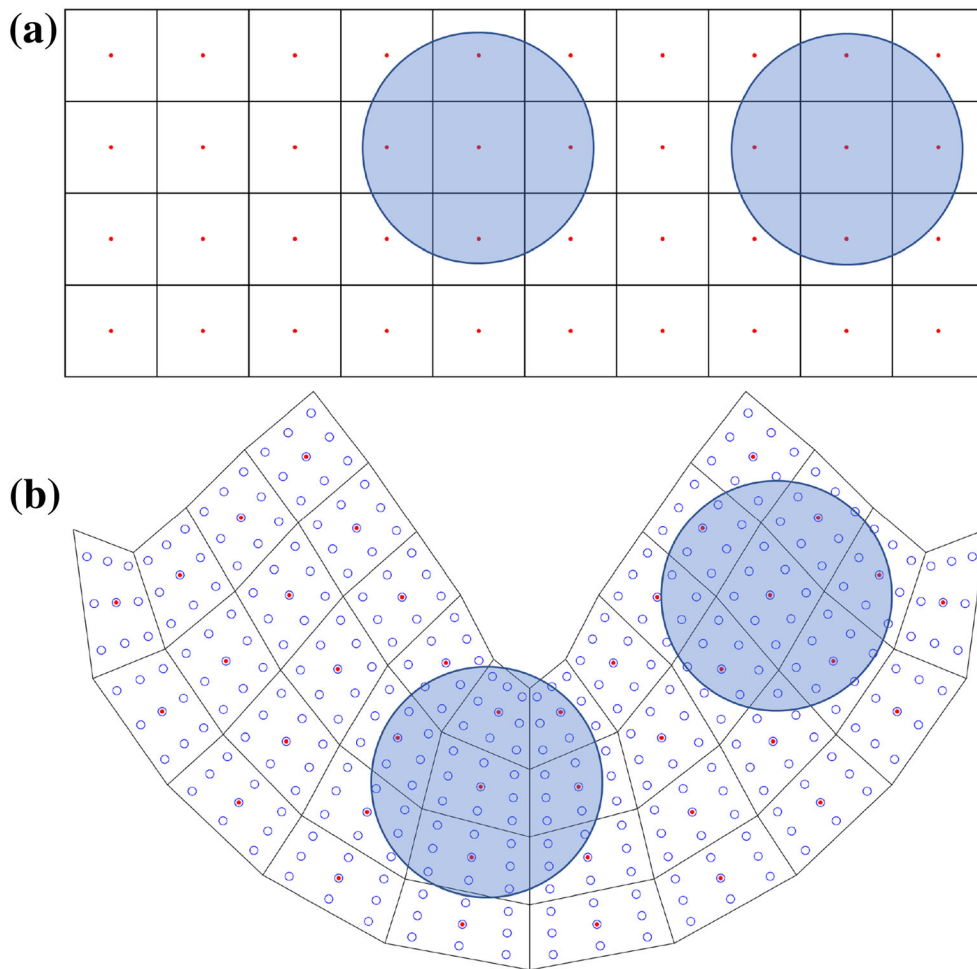
(a)

(b)

Fig. 1 The schemes of local volume calculation for undeformed and deformed configurations

material distribution due to sub-discretization effect. Increasing the number of RVPs provides better precision. As shown by Fig. 1b, the RVPs vary about their positions along with the structural deformation and the number of RVPs inside a local circular area alters simultaneously.

To formulate the new equation of local volume faction calculation, the distance $d_{i,e}$ between any target RVP and the centroid of the current element e is first defined, as:

$$d_{i,e} = \mathrm{r}_{min} - \| \mathbf{p}_i - \mathbf{p}_e \|_2 \tag{3}$$

in which r_{min} is the radius of the circular area, $\| \cdot \|_2$ calculates the vector norm, $\mathbf{p}_i$ represents the i th RVP's coordinate vector, which can be any blue dot in Fig. 1b, and $\mathbf{p}_e$ is the coordinate vector of the e th element's centroid, which may correspond to any red

dot in Fig. 1b. All local material volume fraction constraints are built based on the element centroids, and hence, the local material volume fraction under any deformed configuration is calculated by:

$$vf_e = \frac{\Sigma_{i=1}^{\mathrm{n}} y_i \tilde{v}_i \mathrm{H}\left(d_{i,e}\right)}{\Sigma_{i=1}^{\mathrm{n}} \tilde{v}_i \mathrm{H}\left(d_{i,e}\right)} \tag{4}$$

in which $\mathrm{H}(\cdot)$ is the Heaviside function. n is the total number of RVPs. y_i and $\tilde{v}_i$ are the pseudo density and material volume associated to the i th RVP, respectively. Apparently, $\tilde{v}_i$ is not a constant and depends on the structural deformation condition. Given the need of porosity control, vf_e in Eq. (4) should be smaller than the allowable upper bound $\overline{vf}$.

$$vf_e \leq \overline{vf} \tag{5}$$

3 Nonlinear finite element analysis

3.1 The neo-Hookean model

In this research, we employ the neo-Hookean model (Klarbring and Strömberg 2013) to describe large deformation behavior, which involves both geometric and material nonlinearity. The model is established by its strain energy expression. The strain potential energy is defined as:

$$\phi = \frac{\mu}{2}(I_1 - 3) + \frac{1}{2}\lambda(J - 1)^2 - \mu \ln J \tag{6}$$

where μ and λ are Lame's material parameters.

$$\mu = \frac{E}{2(1 + v)} \tag{7}$$

$$\lambda = \frac{vE}{(1 + v)(1 - 2v)} \tag{8}$$

E and v represent Young's modulus and Poisson's ratio, respectively. The hyperelastic energy model is determined by two invariant terms, I_1 and J, which is demonstrated as follows:

$$I_1 = \mathrm{tr}(\mathbf{C}) \tag{9}$$

$$J = \sqrt{\det(\mathbf{C})} \tag{10}$$

where $\mathbf{C}$ is the right Cauchy-Green deformation tensor.

$$\mathbf{C} = \mathbf{F}^{\mathrm{T}}\mathbf{F} \tag{11}$$

The deformation gradient $\mathbf{F}$ is expressed in Eq. (12).

$$\mathbf{F} = \mathbf{I} + \nabla_0 \mathbf{u} \tag{12}$$

where ∇_0 denotes gradient defined based on the initial configuration. $\mathbf{I}$ represents the identity tensor.

The Green-Lagrangian strain $\mathbf{E}$ is express as:

$$\mathbf{E} = \frac{1}{2}(\mathbf{C} - \mathbf{I}) \tag{13}$$

In hyperelasticity, the second Piola-Kirchoff stress is calculated as follows

$$\mathbf{S} = \frac{\partial \phi}{\partial \mathbf{E}} = 2\frac{\partial \phi}{\partial \mathbf{C}} \tag{14}$$

The elasticity tensor is given by:

$$\mathbf{D} = \frac{\partial^2 \phi}{\partial \mathbf{E}^2} = 4\frac{\partial^2 \phi}{\partial \mathbf{C}^2} \tag{15}$$

3.2 Nonlinear finite element analysis

In this study, all analyses are performed based on the total Lagrangian formulation, wherein all the stress and strain variables correspond to the initial configuration at time $t = 0$. For example, a point P (defined by $\mathbf{X}$) translates to Q (identified by vector $\mathbf{x}$) and the kinematic relation of the point in the initial and current configurations shows below:

$$\mathbf{x} = \mathbf{X} + \mathbf{u}(\mathbf{X}, t) \tag{16}$$

where $\mathbf{u}$ is the displacement, and t is the measurement of time. The Green-Lagrangian strain $\mathbf{E}$ is formulated as:

$$\mathbf{E} = \frac{1}{2}\left(\nabla_0 \mathbf{u} + \nabla_0 \mathbf{u}^{\mathrm{T}} + \nabla_0 \mathbf{u}^{\mathrm{T}}\nabla_0 \mathbf{u}\right) = \frac{1}{2}\left(\mathbf{F}^{\mathrm{T}}\mathbf{F} - \mathbf{I}\right) \tag{17}$$

where ∇_0 denotes gradient operation based on the initial configuration. $\mathbf{I}$ represents the identity tensor. Here, the variance of Green-Lagrangian strain $\mathbf{E}$ is defined as:

$$\overline{\mathbf{E}}(\mathbf{u}, \overline{\mathbf{u}}) = \frac{1}{2}\left(\nabla_0 \overline{\mathbf{u}} + \nabla_0 \overline{\mathbf{u}}^{\mathrm{T}} + \nabla_0 \overline{\mathbf{u}}^{\mathrm{T}}\nabla_0 \mathbf{u} + \nabla_0 \mathbf{u}^{\mathrm{T}}\nabla_0 \overline{\mathbf{u}}\right) \tag{18}$$

in which $\overline{\mathbf{u}}$ is the virtual displacement. To solve the nonlinear FEA problem, the Newton–Raphson method is adopted. The equilibrium equation of Eq. (19) is formulated to describe the kinematics in a static analysis.

$$\int_{\Omega_0} \mathbf{S}(\mathbf{u})\mathbf{E}(\mathbf{u}, \mathbf{u})d\Omega_0 = \int_{\Omega_0} \mathbf{u}^{\mathrm{T}}\mathbf{f}_{\mathrm{b}}d\Omega_0 + \int_{\Gamma_0} \mathbf{u}^{\mathrm{T}}\mathbf{f}_{\mathrm{s}}d\Gamma_0 \tag{19}$$

in which $\mathbf{f}_{\mathrm{b}}$ and $\mathbf{f}_{\mathrm{s}}$ are the body force and surface traction, respectively. $\mathbf{f}_{\mathrm{b}}$ is applied inside the domain Ω_0 and $\mathbf{f}_{\mathrm{s}}$ is employed on the boundary Γ_0. In general, the nonlinear problem is solved by the Newton–Raphson method, and the analysis is divided into numerous steps. Assuming an arbitrary step, equations are achieved by:

$$^{t+\Delta t}\mathbf{u} = {}^{t}\mathbf{u} + \Delta\mathbf{u} \tag{20}$$

$$^{t+\Delta t}\mathbf{E} = {}^{t}\mathbf{E} + \Delta\mathbf{E} \tag{21}$$

$$^{t+\Delta t}\mathbf{S} = {}^{t}\mathbf{S} + \Delta\mathbf{S} \tag{22}$$

and the increment $\Delta\mathbf{E}$ is expressed as:

$$\Delta\mathbf{E} = \frac{1}{2}\Big(\nabla_0(\Delta\mathbf{u}) + \nabla_0(\Delta\mathbf{u})^{\mathrm{T}} + \nabla_0(\Delta\mathbf{u})^{\mathrm{T}}\nabla_0\mathbf{u} + \nabla_0(\mathbf{u})^{\mathrm{T}}\nabla_0(\Delta\mathbf{u})\Big)$$
$$+ \frac{1}{2}\nabla_0(\Delta\mathbf{u})^{\mathrm{T}}\nabla_0(\Delta\mathbf{u}) \tag{23}$$

In Eq. (23), the first and second term have notations as follows:

$$\Delta\mathbf{E}_1 = \frac{1}{2}\Big(\nabla_0(\Delta\mathbf{u}) + \nabla_0(\Delta\mathbf{u})^{\mathrm{T}} + \nabla_0(\Delta\mathbf{u})^{\mathrm{T}}\nabla_0\mathbf{u} + \nabla_0(\mathbf{u})^{\mathrm{T}}\nabla_0(\Delta\mathbf{u})\Big) \tag{24}$$

$$\Delta\mathbf{E}_2 = \frac{1}{2}\nabla_0(\Delta\mathbf{u})^{\mathrm{T}}\nabla_0(\Delta\mathbf{u}) \tag{25}$$

In the FEA formulation of Newton–Raphson method (Belytschko et al. 2014; De Leon et al. 2020; Kim 2015; Wriggers 2008), Eq. (19) can be rewritten as:

$$\int_{\Omega_0} \Delta\mathbf{S}\Delta\mathbf{E}\mathrm{d}\Omega_0 + \int_{\Omega_0} {}^{t}\mathbf{S}\Delta\mathbf{E}_2\mathrm{d}\Omega_0 = \int_{\Omega_0} \Delta\mathbf{u}^{\mathrm{T}t+\Delta t}\mathbf{f}_{\mathrm{b}}\mathrm{d}\Omega_0$$
$$+ \int_{\Gamma_0} \Delta\mathbf{u}^{\mathrm{T}t+\Delta t}\mathbf{f}_{\mathrm{s}}\mathrm{d}\Gamma_0 - \int_{\Omega_0} {}^{t}\mathbf{S}\Delta\mathbf{E}_1\mathrm{d}\Omega_0 \tag{26}$$

According to Eq. (26), the FEA analysis can be rewritten as:

$$(\mathbf{K}_{\mathrm{L}} + \mathbf{K}_{\mathrm{N}})\Delta\mathbf{u} = \mathbf{f}_{\mathrm{ext}} - \mathbf{f}_{\mathrm{int}} \tag{27}$$

where

$$\mathbf{K}_{\mathrm{L}} = \int_{\Omega_0} \mathbf{B}_{\mathrm{L}}^{\mathrm{T}}\mathbf{D}\mathbf{B}_{\mathrm{L}}\mathrm{d}\Omega_0 \tag{28}$$

$$\mathbf{K}_{\mathrm{N}} = \int_{\Omega_0} \mathbf{B}_{\mathrm{N}}^{\mathrm{T}\,t}\mathbf{S}\mathbf{B}_{\mathrm{N}}\mathrm{d}\Omega_0 \tag{29}$$

$$\mathbf{f}_{\mathrm{ext}} = \int_{\Omega_0} \Delta\mathbf{u}^{\mathrm{T}\,t+\Delta t}\mathbf{f}_{\mathrm{b}}\mathrm{d}\Omega_0 + \int_{\Gamma_0} \Delta\mathbf{u}^{\mathrm{T}\,t+\Delta t}\mathbf{f}_{\mathrm{s}}\mathrm{d}\Gamma_0 \tag{30}$$

$$\mathbf{f}_{\mathrm{int}} = \int_{\Omega_0} \mathbf{B}_{\mathrm{N}}^{\mathrm{T}\,t}\mathbf{S}\mathrm{d}\Omega_0 \tag{31}$$

where $\mathbf{B}_{\mathrm{L}}$ and $\mathbf{B}_{\mathrm{N}}$ are displacement–strain matrices related to linear and nonlinear terms, respectively

(Zhang et al. 2020). $\mathbf{S}$ is the second Piola-Kirchoff stress, and $\mathbf{D}$ is the material elasticity tensor. The general nonlinear FEA equation of Eq. (27) is given by:

$$\mathbf{K}_{\mathrm{T}}\Delta\mathbf{u} = \mathbf{r} \tag{32}$$

where $\mathbf{K}_{\mathrm{T}}$ is tangent stiffness and $\mathbf{r}$ is the residual force. The structural status is analyzed by solving Eq. (32) step by step.

3.3 Structural stabilization scheme

As previously mentioned, structural instability in FEA is the most challenging issue in density-based topology optimization due to mesh over distortion. With the classic SIMP interpolation, void elements and low-density elements co-exist that have penalized close-to-zero stiffness, and consequently, severe local mesh distortions tend to happen, leading to negatively defined global structural stiffness matrices. To circumvent this problem, inspired by Wang's work (Wang et al. 2014a), the strain energy of an element is reformulated with:

$$\overline{\phi} = \phi\left(\overline{\overline{\rho}}_e\mathbf{u}_e\right) \tag{33}$$

ϕ is the strain energy as defined in Eq. (6). The subscript e denotes the element index. The parameter $\overline{\overline{\rho}}_e$ is mapped through Heaviside projection from the original $\overline{\rho}_e$. The smoothed Heaviside projector is employed as Eq. (34) (Wang et al. 2011).

$$\overline{\overline{\rho}}_e = \frac{\tanh(\beta\eta) + \tanh\big(\beta(\overline{\rho}_e - \eta)\big)}{\tanh(\beta\eta) + \tanh(\beta(1-\eta))} \tag{34}$$

$\eta \in (0, 1)$ is the projection threshold, and β is the parameter controlling sharpness of the projection curve. Namely, if the pseudo physical density $\overline{\rho}_e$ falls below the threshold, it will be transformed into a small positive value; in contrast, when $\overline{\rho}_e$ is larger than the threshold, $\overline{\rho}_e$ projects to 1. In implementation, due to the severe distortion occurring for pseudo physical densities ranging from 0.1 to 0.3 (Luo et al. 2015), the parameter η in Eq. (34) is assigned 0.215 based on numerical experiments. The projection sharpness control parameter β is set as 500. Referring to Eq. (33), the low-density elements' nodal displacements reduce significantly with the multiplication of the projected element densities, which ensure the

global structural stiffness being positive definite. The above displacement reduction, however, scales up the element tangent stiffness, but the low-density elements still contribute little to the overall structural stiffness because of the SIMP interpolation of Eq. (41).

4 Topology optimization

4.1 Formulating topology optimization for end-compliance minimization

In general, the minimization of structural end-compliance, namely the maximization of structural stiffness, is defined as the objective for hyperelastic structure optimization. The end-compliance minimization problem with maximum local material volume fraction constraint is mathematically formulated as follows:

$$\min_{0 < \rho \leq 1} \psi(\boldsymbol{\rho}) = \mathbf{f}_{\text{ext}}^{\text{T}} \mathbf{u}$$
$$s.t. \mathbf{r} = \mathbf{f}_{\text{ext}} - \mathbf{f}_{\text{int}} = 0 \tag{35}$$
$$\tilde{V} - 1 \leq 0$$

where $\mathbf{r}$, $\mathbf{f}_{\text{ext}}$ and $\mathbf{f}_{\text{int}}$ represent residual, external and internal force of the Newton–Raphson method, respectively. $\mathbf{u}$ denotes the displacement. $\tilde{V}$ is the aggregated local material volume fraction measurement.

The topology optimization problem is solved by the method of moving asymptotes (MMA) (Svanberg 1987). Hence, the gradients of the objective and constraint functions with respect to design variables play a critical role. The sensitivity of the augmented objective function with respect to $\overline{\overline{\rho}}_e$ is expressed as follows:

$$\frac{\partial L}{\partial \overline{\overline{\rho}}_e} = \mathbf{f}_{\text{ext}}^{\text{T}} \frac{\partial \mathbf{u}}{\partial \overline{\overline{\rho}}_e} + \boldsymbol{\lambda}^{\text{T}} \left(\frac{\partial \mathbf{r}}{\partial \overline{\overline{\rho}}_e} + \frac{\partial \mathbf{r}}{\partial \mathbf{u}} \frac{\partial \mathbf{u}}{\partial \overline{\overline{\rho}}_e} \right) \tag{36}$$

To eliminate the unknown $\frac{\partial \mathbf{u}}{\partial \overline{\overline{\rho}}_e}$, the adjoint equation is given by:

$$\mathbf{f}_{\text{ext}} = -\frac{\partial \mathbf{r}}{\partial \mathbf{u}} \boldsymbol{\lambda} \tag{37}$$

The tangent stiffness can be obtained by:

$$\mathbf{K}_{\text{T}} = -\frac{\partial \mathbf{r}}{\partial \mathbf{u}} \tag{38}$$

According to Eq. (37) and Eq. (38), the adjoint equation is derived as follow:

$$\mathbf{f}_{\text{ext}} = \mathbf{K}_{\text{T}} \boldsymbol{\lambda} \tag{39}$$

Here, the sensitivity of the objective function is rewritten as:

$$\frac{\partial L}{\partial \overline{\overline{\rho}}_e} = \boldsymbol{\lambda}^{\text{T}} \frac{\partial \mathbf{r}}{\partial \overline{\overline{\rho}}_e} \tag{40}$$

For topology optimization with SIMP method, the material interpolation is shown as follows:

$$E(\overline{\overline{\rho}}_e) = E_{\min} + (E_0 - E_{\min}) \overline{\overline{\rho}}_e^p \tag{41}$$

where E_0 is the Young's modulus of the solid material and $E_{\min}$ equals $10^{-9} \times E_0$. p is the penalty of the SIMP interpolation. Then, the energy density is reformulated based on the structural stabilization scheme of Eq. (34), the hyperelasticity model of Eq. (6), and the interpolation of Eq. (41).

$$\phi = \left(E_{\min} + (E_0 - E_{\min}) \overline{\overline{\rho}}_e^p \right) \cdot \phi \left(\overline{\overline{\rho}}_e \mathbf{u}_e \right)|_{E=1} \tag{42}$$

where $\phi \left(\overline{\overline{\rho}}_e \mathbf{u}_e \right)|_{E=1}$ is the unit hyperelastic energy with respect to $E = 1$. The internal force is calculated by Eq. (43).

$$\mathbf{f}_{\text{int}} = \left(E_{\min} + (E_0 - E_{\min}) \overline{\overline{\rho}}_e^p \right) \cdot \mathbf{f}_{\text{int}} \left(\overline{\overline{\rho}}_e \mathbf{u}_e \right)|_{E=1} \tag{43}$$

$\mathbf{f}_{\text{int}} \left(\overline{\overline{\rho}}_e \mathbf{u}_e \right)|_{E=1}$ is the unit internal force and calculated by Eq. (31) in term of $E = 1$. According to Eq. (40) and Eq. (43), the sensitivity of objective is written as follows

$$\frac{\partial L}{\partial \overline{\overline{\rho}}_e} = -\boldsymbol{\lambda}^{\text{T}} \left(p(E_0 - E_{\min}) \overline{\overline{\rho}}_e^{p-1} \right) \cdot \mathbf{f}_{\text{int}} \left(\overline{\overline{\rho}}_e \mathbf{u}_e \right)|_{E=1} \tag{44}$$

In general, the density filter is employed to avoid checkerboard patterns and the involved convolution operation transforms the design variable ρ into:

$$\tilde{\rho}_e = \frac{\Sigma_{i \in N_e} H_i \rho_i}{\Sigma_{i \in N_e} H_i} \tag{45}$$

where ρ_i is design variable corresponding to element i. The weight function H_i defines as follows:

$$H_i = r_{\text{f}} - \|\mathbf{c}_i - \mathbf{c}_{e2}\| \tag{46}$$
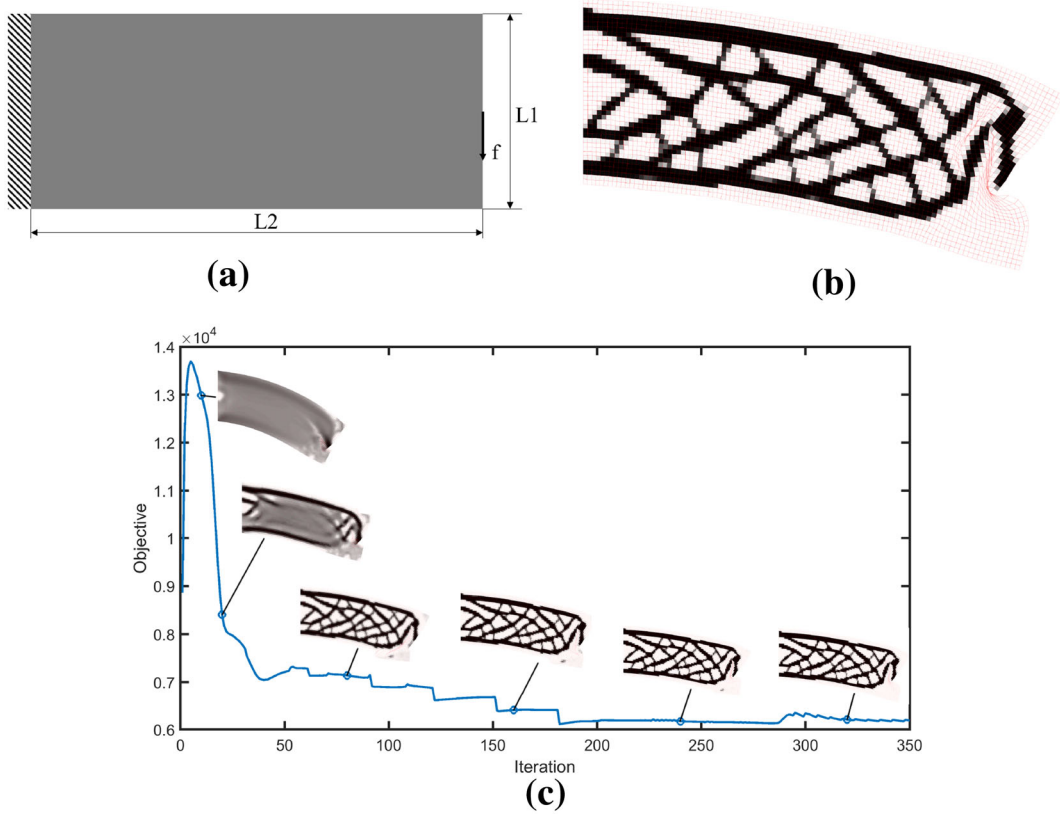
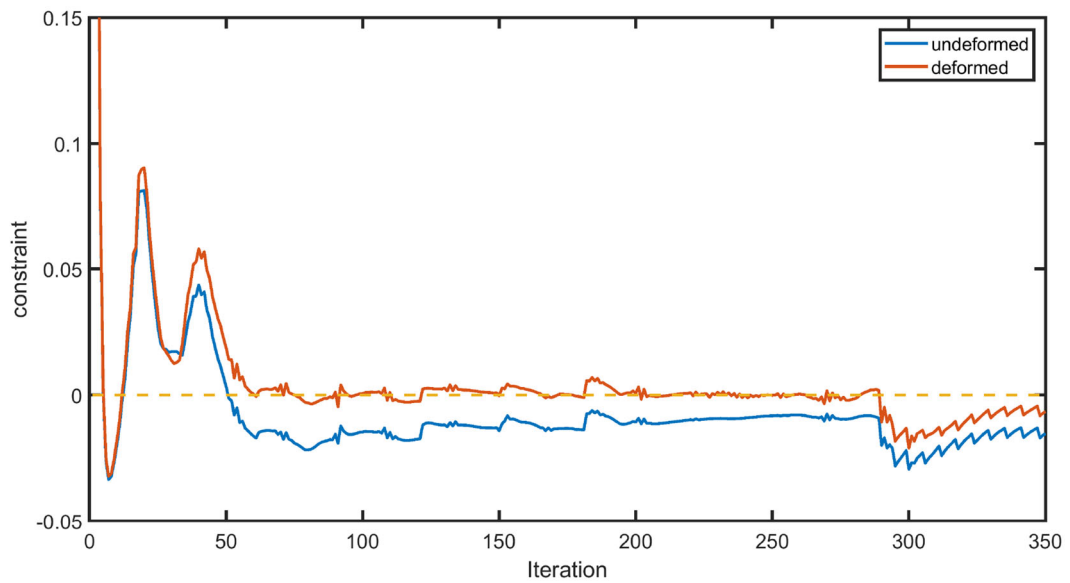Fig. 2 The porous infill cantilever structure

Fig. 3 Converging history of the maximum local volume fraction constraint for the undeformed and deformed state
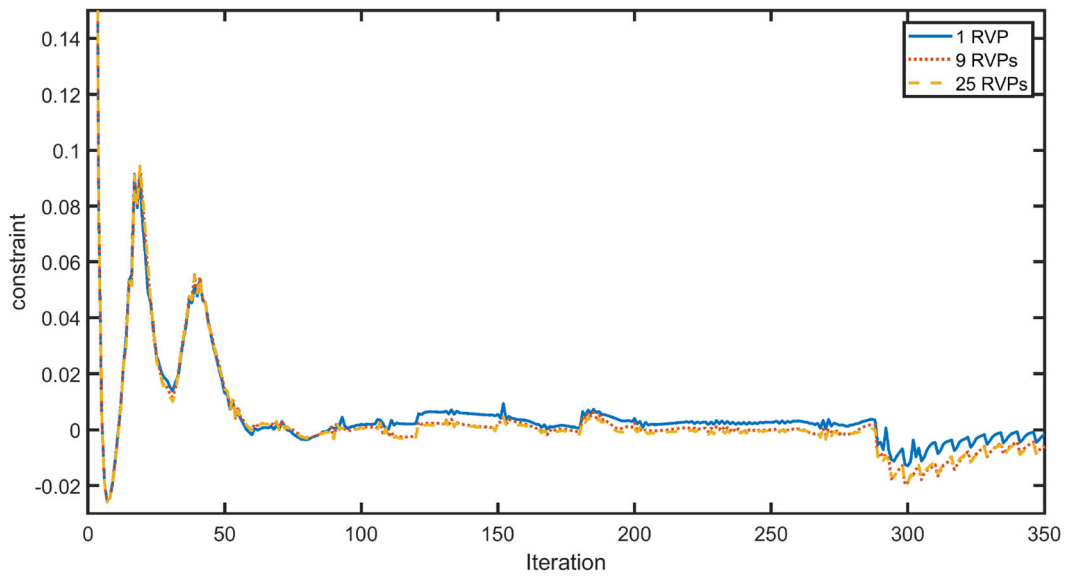
Fig. 4 The deformed local material volume control with 1, 9 and 25 RVPs for an element
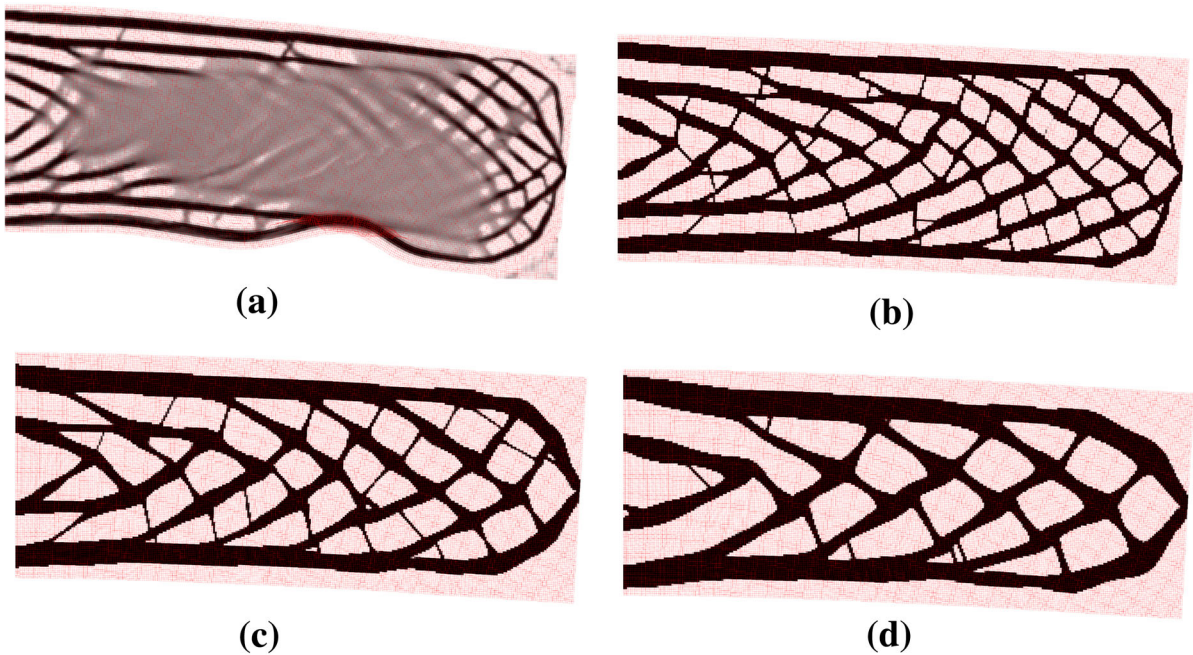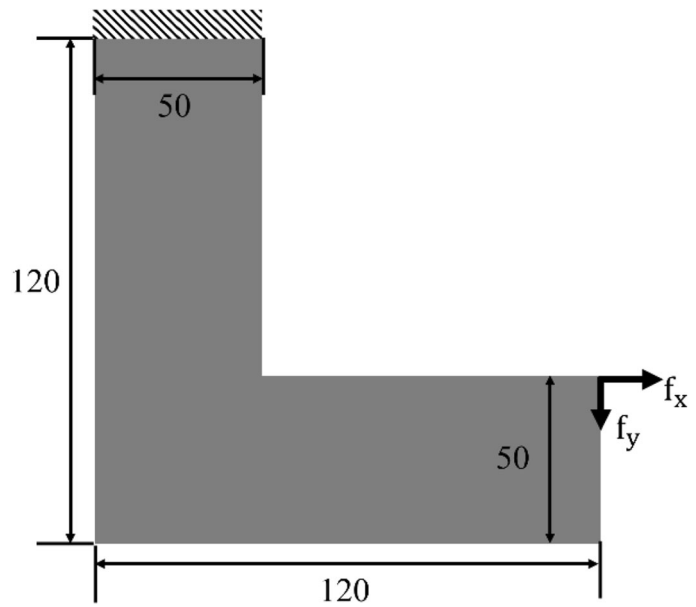

(a)

(b)

(c)

(d)

Fig. 5 The cantilever (300*120 elements) optimization results with different local volume influence radii: **a** r_{min} = 9; **b** r_{min} = 15; **c** r_{min} = 21; **d** r_{min} = 27

in which $\mathbf{c}_i$ and $\mathbf{c}_e$ are the centroid coordinates of element i and e, respectively. r_f is the filter radius. To eliminate blurred boundary from the optimization result, Heaviside projection (Eq. (34)) is made

following the smoothing filter, which projects the intermediate densities ($\tilde{\rho}_e$) into pseudo physical density $\overline{\tilde{\rho}}_e$. The sensitivity of the objective function related to design variables (ρ_e) is written by the chain rule, as:

Fig. 6 The L-bracket example

$$\frac{\partial L}{\partial \rho_e} = \frac{\partial L}{\partial \overline{\tilde{\rho}}_e} \frac{\partial \overline{\tilde{\rho}}_e}{\partial \tilde{\rho}_e} \frac{\partial \tilde{\rho}_e}{\partial \rho_e} \tag{47}$$

4.2 Aggregation of the maximum local volume fraction constraints

For topology optimization, too many local constraints lead to difficulties to the convergence speed and stability, and hence, Eq. (5) should be transformed into a global and derivable expression. In this work, the P-norm method is employed to aggregate the local volume fraction constraints:

$$V = \left[\Sigma_{e=1}^{\text{nele}} \left(\frac{vf_e}{\overline{vf}} \right)^{\mathbb{P}} \right]^{1/\mathbb{P}} \leq 1 \tag{48}$$

where nele is the total number of elements.

The P-norm formula in Eq. (48) is equivalent to applying the many local constraints of Eq. (5) when parameter $\mathbb{P}$ is large enough. However, a too large $\mathbb{P}$ value causes high nonlinearity of the optimization problem, leading to numerical difficulties for a stable convergence. Hence, a medium $\mathbb{P}$ value is oftentimes employed but the P-norm approximated maximum local volume fraction cannot accurately reflect the exact maximum local value. To remedy this issue, the corrected P-norm aggregation is imposed.

According to (Yang et al. 2018; Xu et al. 2021a, b), the P-norm aggregation is iteratively corrected as:

$$\tilde{V} = cp \cdot V \leq 1 \tag{49}$$

wherein the parameter cp is given by Eq. (50) to eliminate the gap between the P-norm approximated maximum local volume fraction and the exact maximum local volume fraction.

$$cp_{\text{k}} = q_{\text{k}} \frac{\max(vf_e)_{\text{k}}}{\overline{vf} \cdot V} + (1 - q_{\text{k}})cp_{\text{k}-1} \tag{50}$$

in which k is the iteration index, and $q_{\text{k}} \in (0, 1]$ is used to balance cp_{k} and $cp_{\text{k}-1}$.

As of the constraint function in Eq. (49), the derivative of the constraint function with respect to the design variable is derived as:

$$\frac{\partial \tilde{V}}{\partial \rho_{\text{e}}} = \frac{\partial}{\partial \rho_{\text{e}}} \left(cp \cdot \left[\Sigma_{e=1}^{\text{nele}} \left(\frac{vf_e}{\overline{vf}} \right)^{\mathbb{P}} \right]^{\frac{1}{\mathbb{P}}} \right)$$

$$= cp \cdot \left[\Sigma_{e=1}^{\text{nele}} \left(\frac{vf_e}{\overline{vf}} \right)^{\mathbb{P}} \right]^{\frac{1}{\mathbb{P}}-1} \Sigma_{e=1}^{\text{nele}} \left[\left(\frac{vf_e}{\overline{vf}} \right)^{\mathbb{P}-1} \frac{1}{\overline{vf}} \frac{\Sigma_{i=1}^{n} \left(\frac{\partial y_i}{\partial \rho_e} \tilde{v}_i \text{H}(d_{i,e}) \right)}{\left(\Sigma_{i=1}^{n} \tilde{v}_i \text{H}(d_{i,e}) \right)} \right] \tag{51}$$

5 Numerical examples

In this section, the proposed method is validated by the benchmark examples. The neo-Hookean model is used to describe the large deformation behavior, addressing both the geometric and material nonlinearities. The Young's modulus is 3×10^9, and Poisson's ratio is 0.4. In the FEA algorithm, the convergence criteria (10^{-3}) is measured by the ratio of residual force to the original value in the Newton–Raphson method. And for the topology optimization process, the structure is accepted when the ratios of objective changes fall below 10^{-2} for 6 consecutive iterations. The penalty p of Eq. (41) is chosen 3. $\mathbb{P}$ of P-norm is 8 for cases. q_k of Eq. (50) defines 0.5. In Heaviside projection for overcoming blur boundary, the threshold (η) is 0.5, and the sharpness (β) increases by 30% for every 30 iterations.
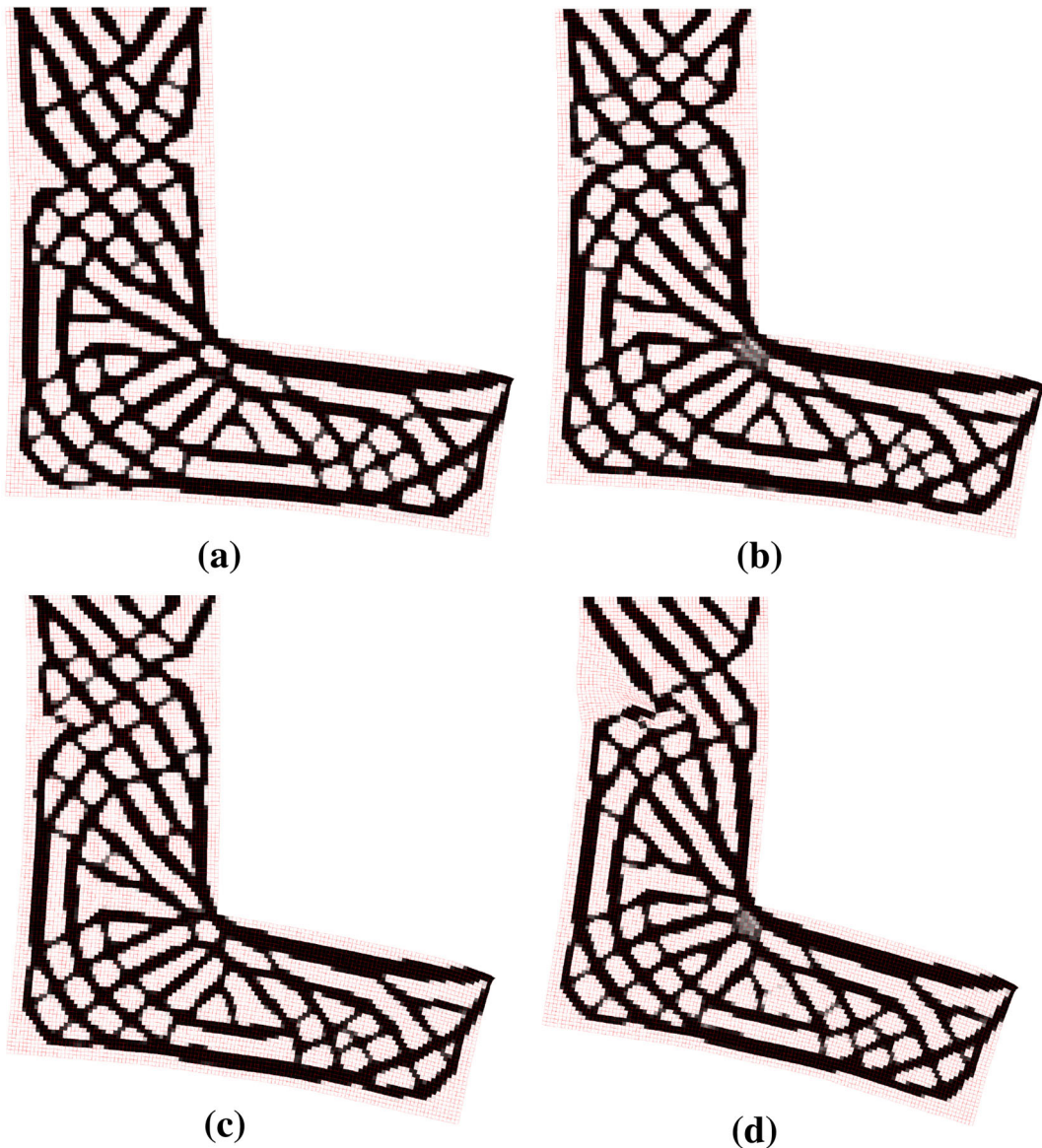
Fig. 7 L-bracket optimization results with different loading combinations: **a** $f_x = 300$ and $f_y = 160$; **b** $f_x = 300$ and $f_y = 200$; **c** $f_x = 300$ and $f_y = 240$; **d** $f_x = 300$ and $f_y = 280$

Fig. 8 The cantilever example

5.1 Case 1

As illustrated in Fig. 2a, the 2D cantilever beam is studied, wherein the left edge is clamped and a concentrated load (f = 320) is applied at midpoint of the right edge. The whole domain is discretized by 100×40 uniform grids. The optimization problem is to minimize the end-compliance subject to the local material volume fraction limit of 0.6 for the deformed state and global materials fraction of 0.6. The local volume influence radius $r_{min} = 6.5$ is prescribed. The optimized porous infill structure is shown in Fig. 2b and the converging history of objective value is presented in Fig. 2c. Figure 3 depicts the converging history of the maximum local material volume constraint, which is calculated with Eq. (52).

$$cp \cdot \left[\Sigma_{e=1}^{nele} \left(\frac{vf_e}{\overline{\overline{vf}}} \right)^{\mathbb{P}} \right]^{1/\mathbb{P}} - 1 \leq 0 \qquad (52)$$

The constraint satisfaction threshold is marked by the dashed line in Fig. 3. It can be seen that all local material volumes in the deformed state fall below the upper limit upon convergence, indicating the effectiveness of the proposed maximum local volume control method. For the comparison purpose, the local volume fractions for the undeformed state along the iterations are shown in the same figure and it is clearly indicated that, the maximum local material volume
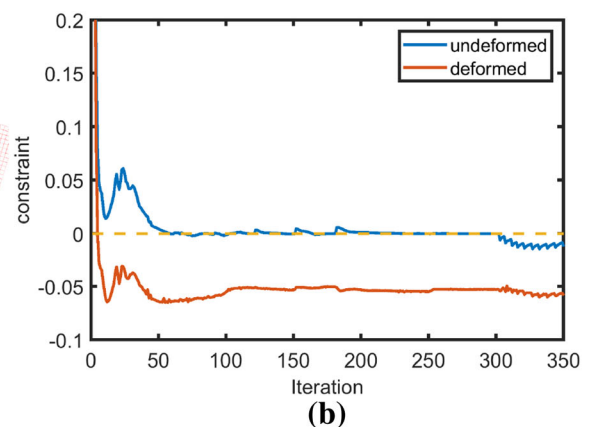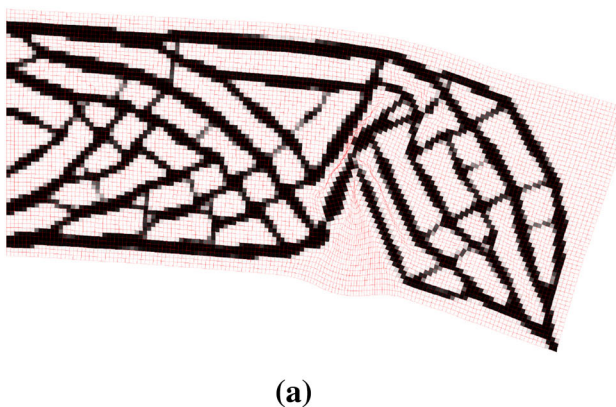

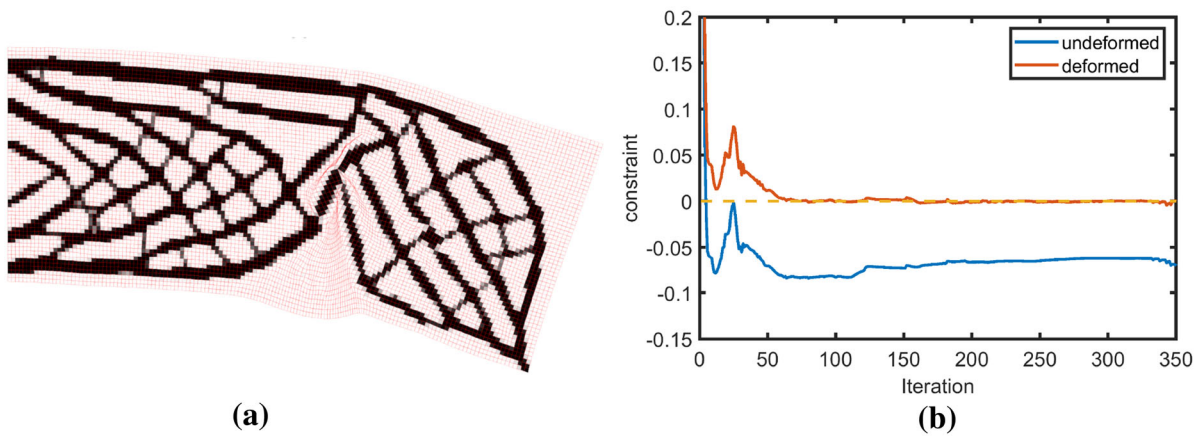**Fig. 9** The optimized structure and converging history for setup (i)

Fig. 10 The optimized structure and converging history for setup (ii)
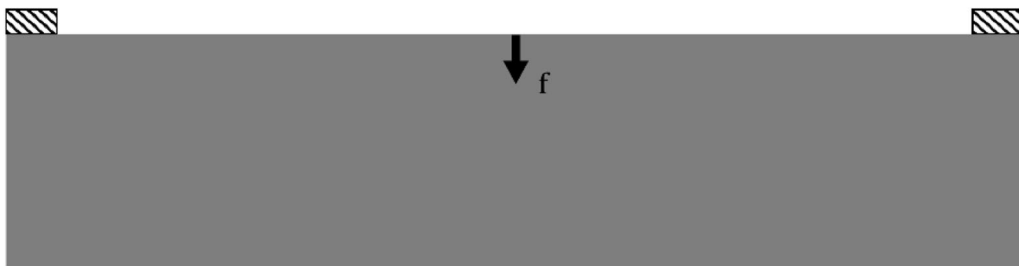

Fig. 11 The long beam example

fractions for the deformed and undeformed states differ significantly. It is unrealistic to simultaneously constrain the maximum local material volumes for the deformed and undeformed states with a single constraint, and therefore, it is significant to develop the method for deformed local material volume measurement and control. In general, more RVPs would increase the accuracy of maximum local material volume control. Figure 4 depicts the constraint satisfaction statuses with different amounts of RVPs inside an element, which gives the evidence that 9 RVPs can provide sufficiently accuracy.

Then, the impact of the local volume influence radius is explored. In Fig. 5, the optimized structures with deformed maximum local volume fraction constraint are demonstrated with different local influence radii. For the large radii of $r_{min} = 15$, $r_{min} = 21$ and $r_{min} = 27$ in Fig. 5b, c and d, the clear-cut black and white structural designs are derived. However, in Fig. 5a, the algorithm fails to converge to a clear-cut design due to the divergence of Newton–Raphson

method when analyzing the structural response involving buckling phenomenon. It is shown in the results that the local influence radius affects the sizes of holes and structural components. A smaller influence radius results in smaller-sized structural components, which are prone to buckling failure that degrades the robustness of the finite element program. Adding buckling constraint may alleviate the above issue, but a more likely result is the conflict to the maximum local volume fraction constraint since the buckling constraint adds materials to strengthen the local compressing structures. Hence, a small local volume influence radius is not preferred, even though increasing the influence radius reduces the level of structural porosity.

5.2 Case 2

This case studies the porous infill design of the L-bracket structure. The optimization problem is to minimize the end-compliance subject to the local and
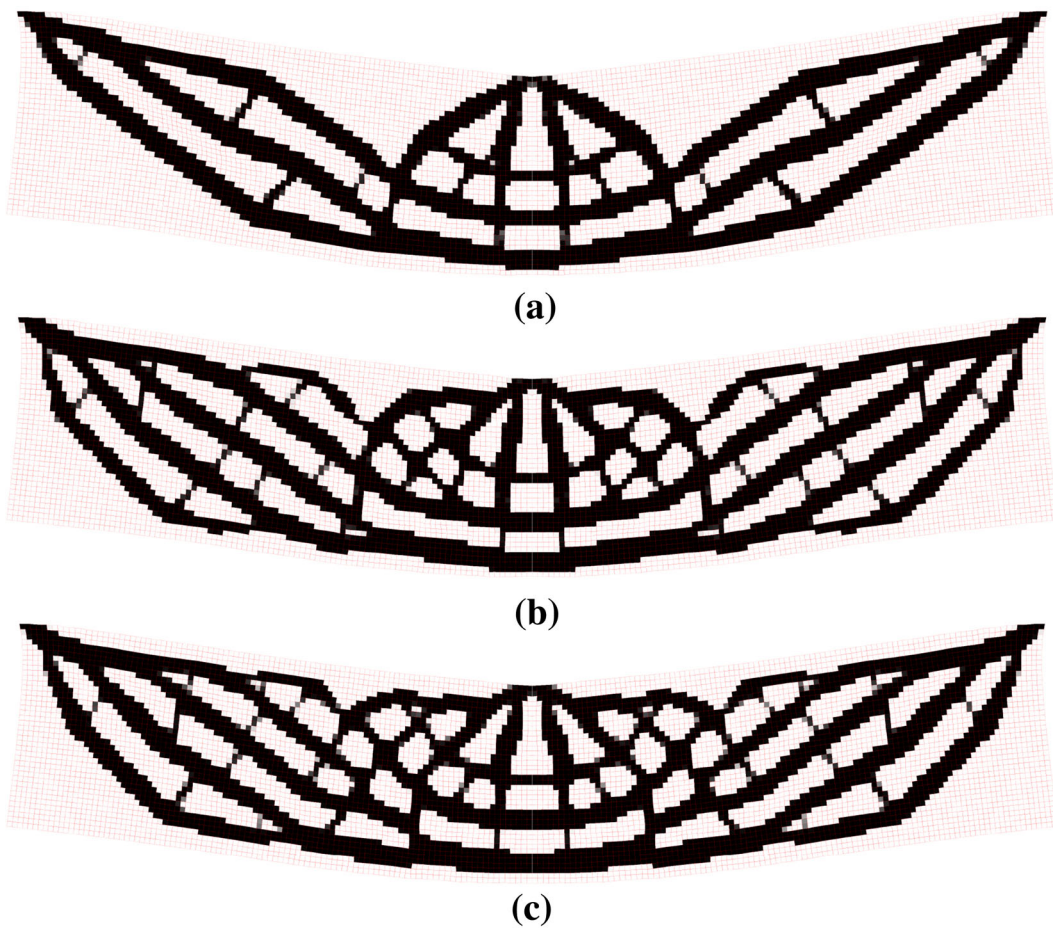
Fig. 12 Porous infill optimization results of the long beam structure

global material volume fraction limit of 0.7 for the deformed state. The local volume influence radius equals $r_{min} = 6.5$. The boundary conditions are depicted in Fig. 6, wherein two concentration forces are loaded to the structure and their magnitudes are varied to derive a series of porous designs; see Fig. 7. From Fig. 7a-d, the loading magnitude in x-direction remains unchanged while the loading magnitudes in y-direction changes from 160 to 280. First of all, regardless of the loading combination, the optimization processes successfully converge with well-controlled maximum local volume fractions. It is important to note that, the x-direction loading reduces the compression load at the left supporting leg of the L-bracket, so that the structure can undergo relatively large deformation while not appearing buckling failure. It is also observed from the results that, the

increased y-direction loading creates more long and slender bar structures for anisotropic structure strengthening instead of the isotropic porosity.

5.3 Case 3

In this case, the cantilever example (Fig. 8) is studied again by considering a combining force acting at the right-bottom corner. The force is composed of a horizontal component of f_x and a vertical component f_y. The horizontal force f_x decreases the element compression along the bottom edge to prevent buckling at relatively small deformation stages. In this way, the vertical force f_y can lead to large structural deformation. For this example, the maximum local volume constraints for the deformed and undeformed states are simultaneously imposed. Two optimization
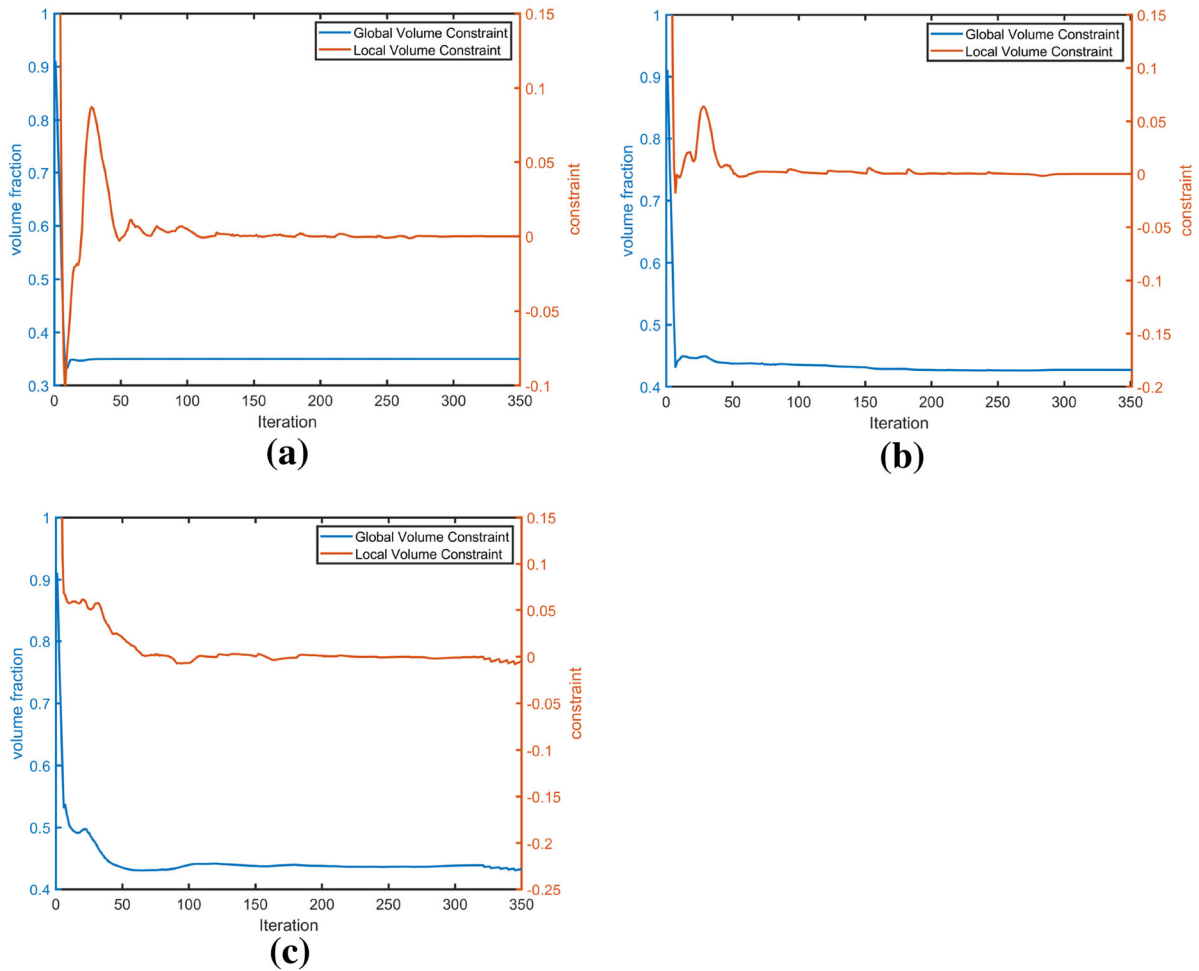
Fig. 13 The converging histories of the constraints

setups are considered with (i) undeformed local volume fraction limit of 0.55, deformed local volume fraction limit of 0.60, and global material fraction limit of 0.6 ($f_x = 160, f_y = 280$), and (ii) undeformed local volume fraction limit of 0.60, deformed local volume fraction limit of 0.55, and global material fraction limit of 0.6 ($f_x = 160, f_y = 280$). The design domain is discretized by 150×60 elements and the local influence radius equals 6.5. Then, the optimization results are shown in Fig. 9 for setup (i) and Fig. 10 for setup (ii). First of all, the optimization processes successfully converge with well-controlled maximum local volume fractions for both deformed and undeformed states. It is interesting to see that regardless of targeting the undeformed or deformed state, the

constraint with smaller volume fraction upper limit are prone to activation while the other constraint remains deactivated for most of the iterations. Hence, imposing only one constraint with the smaller volume fraction upper limit would be sufficient.

5.4 Case 4

In case 4, we try to exploit the long beam example subject to both global volume constraint and deformed maximum local volume constraint. In Fig. 11, the boundary condition is depicted: the upper-left and upper-right corners are fixed, and a concentrated force ($f = 110$) is applied to the midpoint of the top edge. The design domain is discretized by 200×40
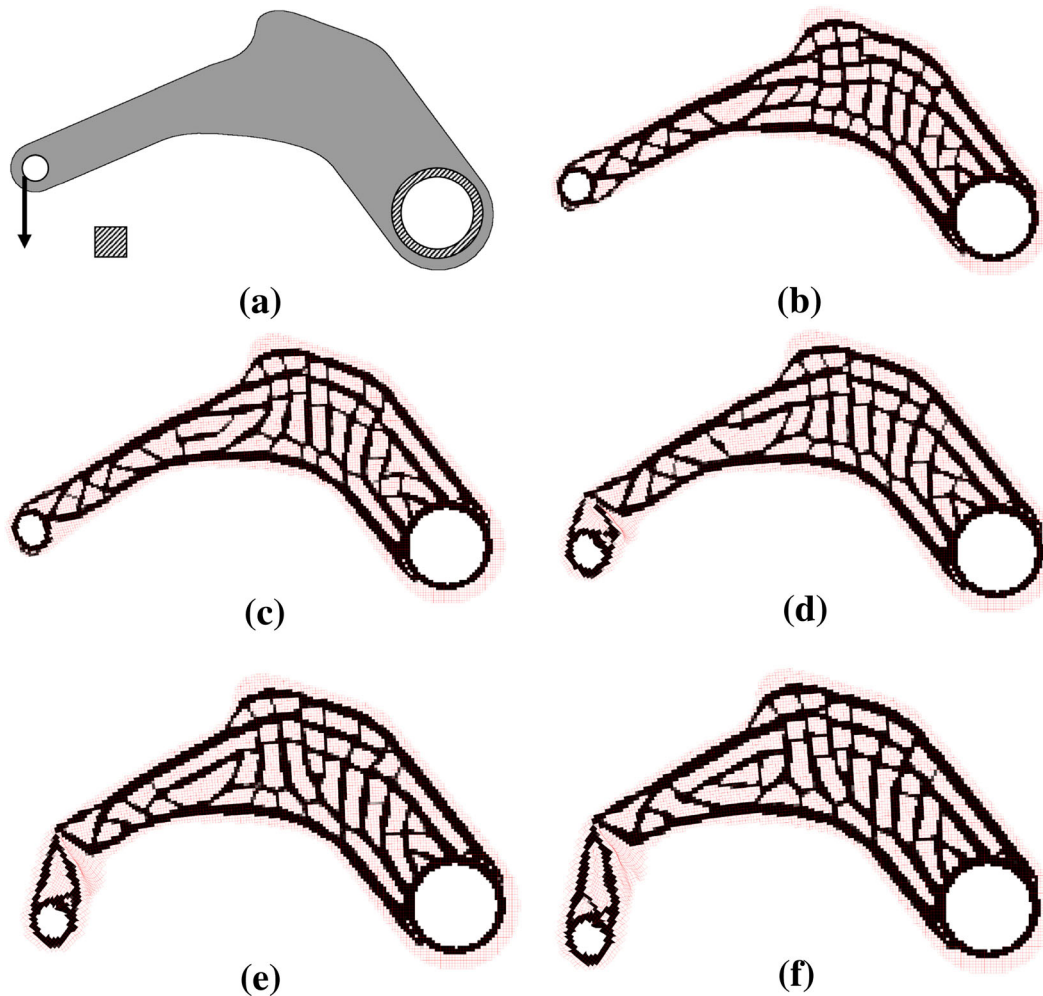
Fig. 14 Connection rod optimization subject to different loading options

elements. The local volume fraction upper limit for deformed state is 70%, and the local influence radius equals 6.5. Three sets of global volume fraction upper limits of 35%, 45% and 55% are explored and the corresponding optimization results are presented in Fig. 12a, Fig. 12b, and Fig. 12c, respectively. It is found that with the increased global material volumes, increasingly more structural details are added to the optimized structure. The convergence histories are plotted in Fig. 13, demonstrating the robust and effective global and local volume control.

5.5 Case 5

Aiming at demonstrating the feasibility of proposed method applied to a practical part, this case focuses on

a connection rod part. As shown in Fig. 14a, the right hole is clamped, and the left hole is applied of a concentrated force. The whole domain is divided into 7158 quadrilateral elements. The optimization objective is to minimize the end-compliance subject to the local and global volume fraction upper bound of 0.6. The local volume influence radius of $r_{min} = 6.5$ is prescribed. From Fig. 14b–f, the loadings are set as 15, 30, 45, 60, 75, respectively. As shown in Fig. 14, the end-point displacement is proportional to the loading magnitude. With the increased loading level, the end point can experience very large deformation owing to the emerged hinge-like connection. Around the hinge connection, lots of elements overlap and over-distort, while the developed finite element solver successfully addresses the overlapping and over-distorted low-
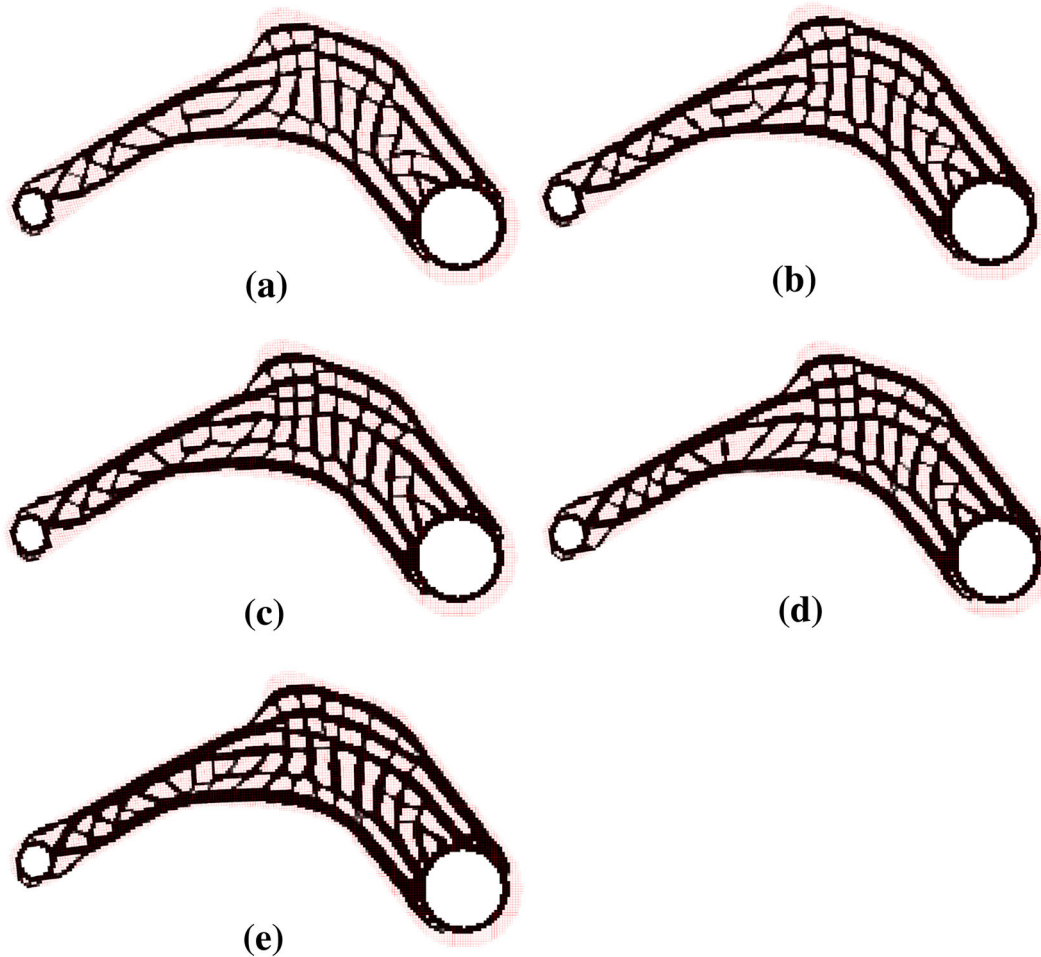
Fig. 15 Connection rod optimization subject to different maximum local volume fraction upper limits. The end-compliance is **a** $\psi = 557.38$, **b** $\psi = 494.61$, **c** $\psi = 459.90$, **d** $\psi = 432.69$, and **e** $\psi = 380.53$

density elements. Then, the right-end, close to the clamping hole, does not show obvious deformations which, therefore, does not experience the buckling issue. In addition, we also explore the design with varying local volume fraction upper limits. Subject to the loading of 30, the optimization results subject to the deformed local volume fraction upper limits of 60%, 65%, 70%, 75%, and 80% are presented in Fig. 15a–e, respectively. The larger local volume fraction deservedly enhances structural performance. It is interesting to see how the hinge-like connection forms with the reduced local volume fraction upper limit.

6 Conclusion

This paper presents a topology optimization method for hyperelastic porous structure design. The RVPs are adopted to tackle the local volume estimation without need of the time-consuming re-meshing. The corrected P-norm method facilitates the accurate control of the maximum local volume fraction. It has been proved in the numerical case study section that the maximum local volume fractions of the deformed and undeformed states can be concurrently controlled with the proposed method.

On the other hand, buckling failure has been identified as the main factor degrading the stability of the proposed method. Thin structural members are generated with the porous structure optimization

method and when imposed of compression load, these thin structures are prone of bucking failure, leading to divergence of Newton's method for analyzing the structural nonlinear response. Increasing the radius for local volume fraction counting results in thicker structural members and increased buckling strength; however, the structural porosity is reduced as well. Adding buckling constraint may alleviate the above issue, but a more likely result is the conflict to the maximum local volume fraction constraint since the buckling constraint adds materials to strengthen the local compressing structure member. Hence, a buckling-free and numerically-stable algorithm for hyperelastic porous structure design still deserves careful investigations.

Declarations

Conflict of interest The authors declare that they have no known competing financial interests or personal relationships that could have appeared to influence the work reported in this paper.

References

Andreassen, E., Lazarov, B., Sigmund, O.: Design of manufacturable 3D extremal elastic microstructure. Mech. Mater. (2014). https://doi.org/10.1016/J.MECHMAT.2013.09.018

Behrou, R., Ghanem, M.A., Macnider, B.C., Verma, V., Alvey, R., Hong, J., Emery, A.F., Kim, H.A., Boechler, N.: Topology optimization of nonlinear periodically microstructured materials for tailored homogenized constitutive properties. Compos. Struct. **266**, 113729 (2021). https://doi.org/10.1016/j.compstruct.2021.113729

Belytschko, T., Liu, W.K., Moran, B., Elkhodary, K.I.: Nonlinear finite elements for continua and structures. Wiley, Chichester, West Sussex, United Kingdon (2014)

Bendsøe, M.P., Kikuchi, N.: Generating optimal topologies in structural design using a homogenization method. Comput. Methods Appl. Mech. Eng. **71**, 197–224 (1988). https://doi.org/10.1016/0045-7825(88)90086-2

Bruns, T.E., Tortorelli, D.A.: An element removal and reintroduction strategy for the topology optimization of structures and compliant mechanisms. Int. J. Numer. Meth. Engng. **57**, 1413–1430 (2003). https://doi.org/10.1002/nme.783

Buhl, T., Pedersen, C.B.W., Sigmund, O.: Stiffness design of geometrically nonlinear structures using topology optimization. Struct Multidisc Optim. **19**, 93–104 (2000). https://doi.org/10.1007/s001580050089

Chen, F., Wang, Y., Wang, M.Y., Zhang, Y.F.: Topology optimization of hyperelastic structures using a level set method. J. Comput. Phys. **351**, 437–454 (2017). https://doi.org/10.1016/j.jcp.2017.09.040

Das, S., Sutradhar, A.: Multi-physics topology optimization of functionally graded controllable porous structures: Application to heat dissipating problems. Mater. Des. **193**, 108775 (2020). https://doi.org/10.1016/j.matdes.2020.108775

De Leon, D.M., Gonçalves, J.F., de Souza, C.E.: Stress-based topology optimization of compliant mechanisms design using geometrical and material nonlinearities. Struct Multidisc Optim. (2020). https://doi.org/10.1007/s00158-019-02484-4

Dou, S.: A projection approach for topology optimization of porous structures through implicit local volume control. Struct Multidisc Optim. **62**, 835–850 (2020). https://doi.org/10.1007/s00158-020-02539-x

Fritzen, F., Xia, L., Leuschner, M., Breitkopf, P.: Topology optimization of multiscale elastoviscoplastic structures. Int. J. Numer. Meth. Eng. **106**, 430–453 (2016). https://doi.org/10.1002/nme.5122

Guest, J.K., Prévost, J.H.: Optimizing multifunctional materials: Design of microstructures for maximized stiffness and fluid permeability. Int. J. Solids Struct. **43**, 7028–7047 (2006). https://doi.org/10.1016/j.ijsolstr.2006.03.001

Guo, X., Zhao, X., Zhang, W., Yan, J., Sun, G.: Multi-scale robust design and optimization considering load uncertainties. Comput. Methods Appl. Mech. Eng. **283**, 994–1009 (2015). https://doi.org/10.1016/j.cma.2014.10.014

Ha, S.-H., Cho, S.: Level set based topological shape optimization of geometrically nonlinear structures using unstructured mesh. Comput. Struct. **86**, 1447–1455 (2008). https://doi.org/10.1016/j.compstruc.2007.05.025

Han, Y., Xu, B., Liu, Y.: An efficient 137-line MATLAB code for geometrically nonlinear topology optimization using bi-directional evolutionary structural optimization method. Struct Multidisc Optim. (2021). https://doi.org/10.1007/s00158-020-02816-9

Huang, X., Radman, A., Xie, Y.M.: Topological design of microstructures of cellular materials for maximum bulk or shear modulus. Comput. Mater. Sci. **50**, 1861–1870 (2011). https://doi.org/10.1016/j.commatsci.2011.01.030

Huang, X., Xie, Y.M., Jia, B., Li, Q., Zhou, S.W.: Evolutionary topology optimization of periodic composites for extremal magnetic permeability and electrical permittivity. Struct Multidisc Optim. **46**, 385–398 (2012). https://doi.org/10.1007/s00158-012-0766-8

Huang, X., Zhou, S., Sun, G., Li, G., Xie, Y.M.: Topology optimization for microstructures of viscoelastic composite materials. Comput. Methods Appl. Mech. Eng. **283**, 503–516 (2015). https://doi.org/10.1016/j.cma.2014.10.007

Kim, N.-H.: Introduction to nonlinear finite element analysis. Springer, New York, NY (2015)

Kim, S., Yun, G.J.: Microstructure topology optimization by targeting prescribed nonlinear stress-strain relationships. Int. J. Plast **128**, 102684 (2020). https://doi.org/10.1016/j.ijplas.2020.102684

Klarbring, A., Strömberg, N.: Topology optimization of hyperelastic bodies including non-zero prescribed displacements. Struct Multidisc Optim. **47**, 37–48 (2013). https://doi.org/10.1007/s00158-012-0819-z

Li, H., Gao, L., Li, H., Tong, H.: Spatial-varying multi-phase infill design using density-based topology optimization. Comput. Method. Appl. Mech. Eng. **372**, 113354 (2020). https://doi.org/10.1016/j.cma.2020.113354

Liu, L., Xing, J., Yang, Q., Luo, Y.: Design of large-displacement compliant mechanisms by topology optimization incorporating modified additive hyperelasticity technique. Math. Probl. Eng. **2017**, 1–11 (2017). https://doi.org/10.1155/2017/4679746

Liu, J., Gaynor, A.T., Chen, S., Kang, Z., Suresh, K., Takezawa, A., Li, L., Kato, J., Tang, J., Wang, C.C.L., Cheng, L., Liang, X., To, Albert.C.: Current and future trends in topology optimization for additive manufacturing. Struct. Multidisc. Optim. **57**, 2457–2483 (2018). https://doi.org/10.1007/s00158-018-1994-3

Liu, B., Cao, W., Zhang, L., Jiang, K., Lu, P.: A design method of Voronoi porous structures with graded relative elasticity distribution for functionally gradient porous materials. Int J Mech Mater Des. (2021). https://doi.org/10.1007/s10999-021-09558-6

Long, K., Wang, X., Liu, H.: Stress-constrained topology optimization of continuum structures subjected to harmonic force excitation using sequential quadratic programming. Struct. Multidisc. Optim. **59**, 1747–1759 (2019). https://doi.org/10.1007/s00158-018-2159-0

Luo, Y., Wang, M.Y., Kang, Z.: Topology optimization of geometrically nonlinear structures based on an additive hyperelasticity technique. Comput. Methods Appl. Mech. Eng. **286**, 422–441 (2015). https://doi.org/10.1016/j.cma.2014.12.023

Ortigosa, R., Ruiz, D., Gil, A.J., Donoso, A., Bellido, J.C.: A stabilisation approach for topology optimisation of hyperelastic structures with the SIMP method. Comput. Method. Appl. Mech. Eng. **364**, 112924 (2020). https://doi.org/10.1016/j.cma.2020.112924

Schmidt, M.-P., Pedersen, C.B.W., Gout, C.: On structural topology optimization using graded porosity control. Struct. Multidisc. Optim. **60**, 1437–1453 (2019). https://doi.org/10.1007/s00158-019-02275-x

Sigmund, O.: A new class of extremal composites. J. Mech. Phys. Solids **48**, 397–428 (2000). https://doi.org/10.1016/S0022-5096(99)00034-4

Svanberg, K.: The method of moving asymptotes—a new method for structural optimization. Int. J. Numer. Meth. Eng. **24**, 359–373 (1987). https://doi.org/10.1002/nme.1620240207

van Dijk, N.P., Langelaar, M., van Keulen, F.: Element deformation scaling for robust geometrically nonlinear analyses in topology optimization. Struct Multidisc Optim. **50**, 537–560 (2014). https://doi.org/10.1007/s00158-014-1145-4

Wang, F.: Systematic design of 3D auxetic lattice materials with programmable Poisson's ratio for finite strains. J. Mech. Phys. Solids **114**, 303–318 (2018). https://doi.org/10.1016/j.jmps.2018.01.013

Wang, F., Sigmund, O.: Numerical investigation of stiffness and buckling response of simple and optimized infill structures. Struct. Multidisc. Optim. **61**, 2629–2639 (2020). https://doi.org/10.1007/s00158-020-02525-3

Wang, F., Lazarov, B.S., Sigmund, O.: On projection methods, convergence and robust formulations in topology optimization. Struct. Multidisc. Optim. **43**, 767–784 (2011). https://doi.org/10.1007/s00158-010-0602-y

Wang, F., Lazarov, B.S., Sigmund, O., Jensen, J.S.: Interpolation scheme for fictitious domain techniques and topology optimization of finite strain elastic problems. Comput. Method. Appl. Mech. Eng. **276**, 453–472 (2014a). https://doi.org/10.1016/j.cma.2014.03.021

Wang, F., Sigmund, O., Jensen, J.S.: Design of materials with prescribed nonlinear properties. J. Mech. Phys. Sol. **69**, 156–174 (2014b). https://doi.org/10.1016/j.jmps.2014.05.003

Wriggers, P.: Nonlinear finite element methods. Springer, Berlin (2008)

Wu, J., Clausen, A., Sigmund, O.: Minimum compliance topology optimization of shell–infill composites for additive manufacturing. Comput. Methods Appl. Mech. Eng. **326**, 358–375 (2017). https://doi.org/10.1016/j.cma.2017.08.018

Wu, J., Aage, N., Westermann, R., Sigmund, O.: Infill optimization for additive manufacturing—approaching bone-like porous structures. IEEE Trans. Visual. Comput. Graphics. **24**, 1127–1140 (2018). https://doi.org/10.1109/TVCG.2017.2655523

Wu, J., Sigmund, O., Groen, J.P.: Topology optimization of multi-scale structures: a review. Struct. Multidisc. Optim. **63**, 1455–1480 (2021). https://doi.org/10.1007/s00158-021-02881-8

Xu, S., Liu, J., Huang, J., Zou, B., Ma, Y.: Multi-scale topology optimization with shell and interface layers for additive manufacturing. Addit. Manuf. **37**, 101698 (2021a). https://doi.org/10.1016/j.addma.2020.101698

Xu, S., Liu, J., Zou, B., Li, Q., Ma, Y.: Stress constrained multi-material topology optimization with the ordered SIMP method. Comput. Methods Appl. Mech. Eng. **373**, 113453 (2021b). https://doi.org/10.1016/j.cma.2020.113453

Yan, J., Guo, X., Cheng, G.: Multi-scale concurrent material and structural design under mechanical and thermal loads. Comput Mech. **57**, 437–446 (2016). https://doi.org/10.1007/s00466-015-1255-x

Yang, D., Liu, H., Zhang, W., Li, S.: Stress-constrained topology optimization based on maximum stress measures. Comput. Struct. **198**, 23–39 (2018). https://doi.org/10.1016/j.compstruc.2018.01.008

Yoon, G.H., Kim, Y.Y.: Element connectivity parameterization for topology optimization of geometrically nonlinear structures. Int. J. Solids Struct. **42**, 1983–2009 (2005). https://doi.org/10.1016/j.ijsolstr.2004.09.005

Zhang, Z., Zhao, Y., Du, B., Chen, X., Yao, W.: Topology optimization of hyperelastic structures using a modified evolutionary topology optimization method. Struct. Multidisc. Optim. (2020). https://doi.org/10.1007/s00158-020-02654-9

Zhang, C., Liu, J., Yuan, Z., Xu, S., Zou, B., Li, L., Ma, Y.: A novel lattice structure topology optimization method with extreme anisotropic lattice properties. J. Comput. Des. Eng. **8**, 1367–1390 (2021a). https://doi.org/10.1093/jcde/qwab051

Zhang, X., Xing, J., Liu, P., Luo, Y., Kang, Z.: Realization of full and directional band gap design by non-gradient topology optimization in acoustic metamaterials. Extreme. Mech. Lett. **42**, 101126 (2021b). https://doi.org/10.1016/j.eml.2020.101126

Zheng, J., Yang, X., Long, S.: Topology optimization with geometrically non-linear based on the element free Galerkin method. Int. J. Mech. Mater. Des. **11**, 231–241 (2015). https://doi.org/10.1007/s10999-014-9257-y